

# **Effects of Thunderstorm Driven Runaway Electrons in the Conjugate Hemisphere: Purple Sprites, Ionization Enhancements and Gamma Rays**

N. G. Lehtinen, U. S. Inan, and T. F. Bell

STAR Laboratory, Stanford University, Stanford, CA 94305

Short title: CONJUGATE RUNAWAY ELECTRON EFFECTS

**Abstract.** The presence of energetic runaway electron beams above thunderstorms is suggested by observations of terrestrial gamma ray flashes [*Fishman et al.*, 1994], as well as theoretical work [*Roussel-Dupré and Gurevich*, 1996; *Lehtinen et al.*, 1999], although such beams have not been directly measured. In this paper, we consider possible measurable effects of such beams in the conjugate hemisphere as a means to confirm their existence and quantify their properties. High density relativistic runaway electron beams, driven upward by intense lightning-generated mesospheric quasi-static electric fields, have been predicted [*Lehtinen et al.*, 2000] to be isotropized and thermalized during their interhemispherical traverse along the Earth's magnetic field lines so that only  $\sim 10\%$  of the electrons which are below the loss cone should arrive at the geomagnetically conjugate ionosphere. As they encounter the Earth's atmosphere, the energetic electrons would be scattered and produce light and ionization, much like a beam of precipitating auroral electrons. A Monte Carlo approach is used to model the interaction of the down-coming electrons with the conjugate atmosphere, including the backscattering of electrons, as well as production of optical and gamma ray emissions and enhanced secondary ionization. Results indicate that these conjugate ionospheric effects of the runaway electron beam are detectable and thus may be used to quantify the runaway electron mechanism.

## 1. Introduction

Energetic runaway electrons above thunderstorms, driven upward by intense quasi-electrostatic fields following a positive cloud-to-ground discharge, has been put forth [Roussel-Dupré *et al.*, 1998 and references therein] as a fundamentally new plasma acceleration process [Gurevich *et al.*, 1992], leading to the generation of gamma ray flashes of terrestrial origin [Fishman *et al.*, 1994; Lehtinen *et al.*, 1996; 1997; 1999]. The possibility of runaway electrons emitting  $\gamma$ -rays above thunderstorms was first suggested by C. T. R. Wilson in 1925 [Wilson, 1925]. However, the possibility of their production in an avalanche mechanism was not considered until recently, following the discovery of luminous high altitude optical flashes [Franz *et al.*, 1990], known now as sprites [e.g., Sentman *et al.*, 1995], and terrestrial gamma ray flashes [Fishman *et al.*, 1994].

Initial work on the runaway avalanche acceleration process led to suggestions that the observed luminosity of sprites may be produced by the energetic runaway electrons [Bell *et al.*, 1995; Taranenko and Roussel-Dupré, 1996; Lehtinen *et al.*, 1997]. However, it was later realized [Lehtinen *et al.*, 1999; Symbalisty *et al.*, 1998] that the early estimates of runaway avalanche rates [Roussel-Dupré *et al.*, 1994] used in much of this work were too high and that while the resultant runaway electron fluxes were sufficiently high to produce the observed flux levels in the terrestrial gamma ray flashes, the optical emissions produced by these electrons were negligible compared to those due to the heating of much larger number of ambient electrons [Lehtinen *et al.*, 1999].

No direct measurements of energetic runaway electron beams have yet been made

and future direct observations are unlikely due to the localized ( $\sim 20$  km lateral size [Lehtinen *et al.*, 1997]) and highly transient ( $\sim 1$  ms duration) nature of the beams as evidenced respectively by the spatial configuration of the driving quasi-static fields and the  $\sim 1$  ms observed durations of terrestrial gamma ray flashes. Nevertheless, the fact that this phenomenon occurs at high altitudes above intense thunderstorms is implied by (i) the observations of terrestrial gamma ray flashes and (ii) by the existence of intense quasi-static fields at these altitudes as evidenced in sprites. Another hint of the possible existence of runaway electrons above lightning discharges is the low altitude satellite measurement reported by *Burke et al.* [1992]. In this measurement, a burst of upward-moving keV electrons was detected at  $\sim 300$  km altitude above an intense hurricane, which could well have been the low-energy tail of the energetic runaway electron beam. The absence of higher-energy electrons in this observation may be due to the fact that the instrument was time-gated with a cycle of one second for each energy bin, so that it could not observe electrons at higher energies especially in view of the relatively short runaway electron burst.

The observation of terrestrial gamma ray flashes by the BATSE  $\gamma$ -ray experiment is one of the most unexpected discoveries by the Compton Gamma-Ray Observatory (CGRO) [*Fishman et al.*, 1994]. The  $\gamma$ -ray photon energy extends above 1 MeV, indicating bremsstrahlung radiation from  $>1$  MeV electrons, consistent with early predictions of upward beams of runaway electrons accelerated by thundercloud fields [*Wilson*, 1925] as well as highly quantitative recent modeling [e.g., *Lehtinen et al.*, 1999]. At least some of the BATSE  $\gamma$ -ray flashes are clearly associated with lightning

discharges [Inan *et al.*, 1996]. To date,  $\sim 70$  terrestrial gamma ray flashes have been observed by BATSE [G. Fishman, *private communication*],  $\sim 1$  per month, in spite of the fact that BATSE's on-board trigger logic has a 64 ms minimum resolution (too long for detection of  $\sim 1$  ms bursts) and the trigger energy range is most often optimized for lower energy phenomena.

The CGRO observations of terrestrial gamma ray flashes imply the presence of  $>1$  MeV electron beams simply because bremsstrahlung radiation from such electrons is the only physically viable source of  $\gamma$ -radiation in the Earth's atmosphere. Quantitative models of the  $\gamma$ -ray production mechanism indicate a runaway beam of 100 keV to 10 MeV electrons radiating  $\gamma$  rays at 60–70 km altitudes [Lehtinen *et al.*, 1999]. Since the upper atmosphere above 70 km is essentially a thin target (i.e., one with decreasing density) for electrons of energy  $>500$  keV, most of these particles must escape upward along the field lines into the radiation belt region, constituting an injected beam of total fluence predicted to be  $10^6$ – $10^7$  el/cm<sup>2</sup> [Lehtinen *et al.*, 1999; 2000].

Observations and modeling of luminous high altitude glows known as sprites [Sentman *et al.*, 1995; Pasko *et al.*, 1997] confirm the existence above thunderstorms of intense quasi-static electric fields of up to  $\sim 1$  kV/m at mesospheric altitudes. These fields are sufficient to produce runaway electron beams via avalanche acceleration [Taranenko and Roussel-Dupré, 1996; Lehtinen *et al.*, 1996; 1997; Roussel-Dupré and Gurevich, 1996], leading to the emission of bremsstrahlung  $\gamma$ -ray flashes [Lehtinen *et al.*, 1999], of intensity consistent with BATSE observations. However, all of the models of this phenomena are highly dependent on the initial conditions [e.g., Roussel-Dupré *et*

*al.*, 1998; *Milikh and Valdivia*, 1999; *Lehtinen et al.*, 1999], because the runaway process is inherently highly nonlinear and the lightning electric fields are highly variable.

Theoretical models have shown that very large charge moments are generally required to produce quasi-static electric fields of sufficient intensity to lead to large enough beam densities leading to observed levels of gamma ray fluxes. Large charge moments in turn mean either that the charge is removed from relatively high ( $>10$  km) altitudes or that very large quantities of charge are removed from lower altitudes. As an example, *Lehtinen et al.* [1999] considered the removal of linearly extended horizontal charge distribution of 1200 C at 10 km altitude, while *Roussel-Dupré and Gurevich* [1996] considered the removal of positive charge of 100 C at 18 km altitude.

It is indeed possible that the runaway electron avalanche occurs only after lightning discharges which remove charge from giant thunderclouds, which, although unusual and rare, have been observed before. The tornado-producing electrical storms with cloud tops at 20 km altitude are discussed by *Vonnegut and Moore* [1958]. The overshooting cloud tops in storm supercells can reach 1–2 km above the tropopause (at  $\sim 18$  km) [*Stolzenburg et al.*, 1998b]. The balloon observations of electric fields in isolated storm supercells, made by *Stolzenburg et al.* [1998b] in strong updraft regions, extend up to  $\sim 13$  km and show the presence of positive charge at altitudes of  $\sim 11$  km and of unknown depth in several soundings. The observations by the same authors [*Stolzenburg et al.*, 1998a] in mesoscale convective systems show the presence of the main positive charge at 12–13 km altitude in measurements extending up to 13.4 km (sounding number 94157.1). In this paper, we consider both point and horizontal disk charge configurations

at 10 km and 15 km altitude and quantify results in terms of the magnitude of removed charge.

It should further be noted that the quoted works provide evidence only for the *existence* of the charges at such high altitudes. The experimental evidence for the removal of charge from such high altitudes is very limited. In the recent measurements of *Krehbiel et al.* [2000] of lightning positions in tornadic and non-tornadic supercell storms, some discharges were detected to occur at altitudes  $>10$  km. However, these transferred little charge and were intracloud rather than cloud-to-ground discharges. Some of these discharges were just parts of extensive lightning flashes draining charge from different parts of thundercloud. Thus, current models of runaway electron acceleration appear to require extreme circumstances in terms of lightning discharge magnitude and altitude from the point of view of experimental data in hand at present time.

The above mentioned highly nonlinear nature of the runaway process underscores the need for direct or indirect measurements in order to confirm its existence and to quantify its properties. Beyond the measurements of gamma ray flashes produced by such beams, direct measurements of the beam are unlikely as mentioned above. However, it is possible that the presence of such beams may be confirmed by means of measurements in the magnetosphere or in the geomagnetically conjugate region. The fate of the runaway electron beam once it escapes the ionosphere was recently considered and it was shown that the high density beam is isotropized and thermalized in a single interhemispheric traverse so that most of the beam electrons remain trapped in the

radiation belts [Lehtinen *et al.*, 2000]. The resultant formation of trapped electron curtains (spread out in longitude and lasting in time) may allow a means to indirectly detect the runaway electron beams in the form of electron flux enhancements in specific narrow  $L$ -shell regions.

In this paper, we consider the physical effects of the precipitating portion of the isotropized beam in the conjugate ionosphere, particularly in terms of production of light, secondary ionization and gamma rays, using a Monte Carlo method to quantify these effects. Our results indicate that the effects of the beam in the conjugate mesosphere are significant and detectable, and that they therefore can be used to confirm the prediction of runaway electron beams at high altitudes above thunderstorms.

The detection of the conjugate effects such as optical emissions should be attempted at a location which is geomagnetically conjugate to a region where large thunderstorms occur frequently. For the mid-western United States, such regions are located in the Pacific Ocean, and are not easily accessible for observations. However, the subionospheric VLF measurements of the secondary ionization produced in the conjugate  $D$  region may be possible on VLF signal paths that traverse the region but which are observed elsewhere. A more convenient location for optical observations is provided by the conjugate land masses of South Africa and Southern Europe with active thunderstorms being common in both hemispheres. In fact, sprites have recently been observed in the Pyrenees region of Southern Europe [Neubert *et al.*, 2000].

In view of the fact that the characteristics of the runaway electron beam are complex nonlinear functions of the thundercloud charge removed in the lightning



discharge, we start our determination of the conjugate effects with the modeling of the generation process of the runaway beam, considered in the next section.

## 2. Formation of the Runaway Electron Beam

The upward driven relativistic electron beam is produced as a result of the quasi-electrostatic field which temporarily exists at high altitudes following positive cloud-to-ground lightning discharges. In this section, we estimate the runaway electron flux entering the ionosphere as a function of the thundercloud charge configuration parameters. In particular, we show that the runaway electron flux depends on the value of the cloud charge in a highly nonlinear manner.

The pre-discharge thundercloud charge configuration is taken to be such that an initial positive charge  $Q$  is located at altitude  $h_+$  and is either concentrated at a point or distributed on a horizontal disk of radius  $a$ . It is accompanied by equal negative charge  $-Q$  at altitude  $h_-$  of the same shape. In this paper, we consider different cases with  $h_+ = 10$  km and  $h_+ = 15$  km, while the negative charge  $-Q$  is assumed to be at  $h_- = 5$  km. The lightning discharge is assumed to lower the positive charge to the ground in time  $\tau = 1$  ms, as shown in Figure 1a, thereby creating the quasi-static field due to uncompensated space charge.

This intense downward pointing quasi-electrostatic field exists until the conducting upper atmosphere relaxes over the course of several to tens of milliseconds, during which time it accelerates seed relativistic electrons (e.g., those produced by cosmic ray showers) upward, which in turn collide with air molecules, producing an avalanche

process, resulting in the formation of an intense runaway electron beam [*Roussel-Dupré et al.*, 1998 and references therein; *Lehtinen et al.*, 1997; 1999].

The quasi-electrostatic field exists for several to tens of milliseconds, which is longer than the time required for relativistic electrons to reach the ionosphere. Accordingly, we can use a stationary continuity equation for calculation of the number density,  $N_R$ , of the runaway electron beam:

$$v_R \frac{dN_R}{dz} = \gamma_R N_R + S_0(z) \quad (1)$$

where  $v_R$  is the runaway velocity,  $\gamma_R$  is the avalanche growth rate,  $S_0(z)$  is the source of energetic electrons from cosmic rays. The growth rate  $\gamma_R > 0$  only when the electric field exceeds the runaway threshold field  $E_t$  [e.g., *Gurevich et al.*, 1992], which is proportional to neutral air density. The Monte Carlo model calculations [*Lehtinen et al.*, 1999] show that the velocity  $v_R \simeq 0.9c$ , while the avalanche rate  $\gamma_R$  is a function of electric field and air density and is nonlinearly dependent on the magnitude and configuration of the removed thundercloud charge. The source  $S_0(z)$ , due to cosmic rays, is proportional to the air density, with  $S_0 = 10 \text{ m}^{-3}\text{s}^{-1}$  at 10 km [*Bell et al.*, 1995]. Note that the density  $N_R$  is a function of spatial coordinates and time, and that its dependence on air density and electric field is implicit via the coefficients  $\gamma_R$  and  $S_0$  in equation (1).

For calculation of the quasi-electrostatic field we assume an exponential air conductivity profile  $\sigma = \sigma_0 e^{z/H}$ , with scale height  $H = 10 \text{ km}$ , as an approximation of the experimental data [*Holzworth et al.*, 1985]. The rather simple conductivity profile used here allows an analytical description of resultant electric field (see below) for the

stationary case considered here, and is sufficient for ballpark estimation of the number density of runaway electrons.

The removal of a positive charge is equivalent to instantaneous placement of a negative charge of equal magnitude at the same location. Since the electric field relaxation time ( $\tau_r = \epsilon_0/\sigma_0$ ) at the altitudes of avalanche is relatively long, the electrostatic field of the just-placed negative charge can be assumed to be the same as in vacuum. The driving quasi-electrostatic field is therefore the sum of the initial stationary field of the thundercloud in the conducting atmosphere and the vacuum field of the equivalent just-placed negative charge, and can be calculated analytically for both the point and disk charge configurations. In this way, the post-discharge electric field is determined predominantly by the negative screening space charge, which is formed in the pre-discharge stage, and the altitude distribution of which depends in form on the magnitude and altitude of  $Q$  and the atmospheric conductivity profile.

For point charges, we note that the Coulomb electrostatic potential of a unit charge in cylindrical coordinates located at  $r_0 = 0$ ,  $z_0 = 0$  in the stratified atmosphere with exponential conductivity profile is [Volland, 1984, p. 34]  $\Phi_{\text{exp}}^{\text{point}}(r, z) = \Phi_{\text{vac}}^{\text{point}}(r, z)e^{-(R+z)/2H}$ , where  $R = \sqrt{r^2 + z^2}$  is the distance between the observation point and the charge and  $\Phi_{\text{vac}}^{\text{point}}(r, z) = (4\pi\epsilon_0 R)^{-1}$  is the potential of a point unit charge in vacuum.

For the case of two separated thundercloud point charges  $\pm Q$  at altitudes  $h_{\pm}$ , we have to take into account the image charges at  $-h_{\pm}$  of values  $Q_{\text{image}\pm} = \pm Qe^{h_{\pm}/H}$ . The

electrostatic potential before the discharge is then given by

$$\begin{aligned} \Phi_{\text{before}}^{\text{point}}(r, z) = Q & \left[ \Phi_{\text{exp}}^{\text{point}}(r, z - h_+) - \Phi_{\text{exp}}^{\text{point}}(r, z - h_-) \right. \\ & \left. - e^{h_+/H} \Phi_{\text{exp}}^{\text{point}}(r, z + h_+) + e^{h_-/H} \Phi_{\text{exp}}^{\text{point}}(r, z + h_-) \right] \end{aligned} \quad (2)$$

The potential immediately after the discharge can be determined from (2) by adding a negative point charge at the location of the removed positive charge and its image:

$$\Phi_{\text{after}}^{\text{point}}(r, z) = \Phi_{\text{before}}^{\text{point}}(r, z) + Q \left[ -\Phi_{\text{vac}}^{\text{point}}(r, z - h_+) + \Phi_{\text{vac}}^{\text{point}}(r, z + h_+) \right] \quad (3)$$

The electrostatic field  $\mathbf{E}$  before and after discharge can then be directly found from  $\mathbf{E} = -\nabla\Phi$ . In the solution of equation (1) we are interested primarily in the vertical electric field  $E_z = -\partial\Phi/\partial z$  along the cylindrical axis  $r = 0$ .

For solution of equation (1), we assume the initial condition of  $N_{R0} = 0$  at some initial altitude  $z_{\text{ini}}$ . For calculations with  $h_+ = 10$  km, we take  $z_{\text{ini}} = 18$  km. At this altitude the ratio  $E/E_t$  after the discharge, derived from (3), is minimal. For the case of an infinitely thin horizontal positive charge at  $h_+ = 15$  km, equation (3) gives a minimum of  $E/E_t$  right above the charge, i.e., at 15 km. We take, however,  $z_{\text{ini}} = h_+ + 2 = 17$  km, to allow for a finite vertical thickness of the charge in the latter case. The upper boundary of the domain of calculations is taken to be at the lower ionosphere boundary, which is at the altitude of 80 km.

The point charge configuration has the disadvantage of having an arbitrarily large electrostatic potential as  $r \rightarrow 0$ . A somewhat more realistic thundercloud charge configuration is a disk of charge. The electrostatic potential of a horizontal disk charge system can be calculated by integrating the potential for the point charge. For a unit

disk charge of radius  $a$ , having a uniform charge density  $(\pi a^2)^{-1}$ , the electrostatic potential along the axis of the system in vacuum is given by

$$\Phi_{\text{vac}}^{\text{disk}}(z) = \frac{1}{\pi a^2} \int_0^a \frac{2\pi r dr}{4\pi\epsilon_0\sqrt{r^2 + z^2}} = \frac{1}{2\pi\epsilon_0 a^2} (\sqrt{a^2 + z^2} - |z|)$$

while the potential in the stratified atmosphere with exponential conductivity profile is given as

$$\begin{aligned} \Phi_{\text{exp}}^{\text{disk}}(z) &= \frac{1}{\pi a^2} \int_0^a \frac{e^{-(\sqrt{a^2+z^2}+z)/(2H)} 2\pi r dr}{4\pi\epsilon_0\sqrt{r^2 + z^2}} \\ &= \frac{H}{\pi\epsilon_0 a^2} e^{-z/(2H)} \left[ e^{-|z|/(2H)} - e^{-\sqrt{a^2+z^2}/(2H)} \right] \end{aligned}$$

The pre-discharge potential for a system of two separated disk charges is a linear combination analogous to equation (2), while the post-discharge potential is given by an expression similar to (3). The vertical component of the quasi-static electric field is once again found from  $E_z = -\partial\Phi/\partial z$ .

For a given amount  $Q$  of total removed charge, the minimum radius of a disk of charge is determined by the requirement that the field in its immediate vicinity before the discharge is lower than the runaway breakdown field  $E_t$ . The minimum radii  $a_{\text{min}}(Q)$  so determined for  $h_+ = 10$  and 15 km are plotted in Figure 2.

The results of calculations of the density of the electron beam entering the magnetosphere based on a numerical solution of equation (1) are shown in Figure 3, for point and disk charges at two different altitudes. We see that the density depends strongly on the discharge value  $Q$ . The first two curves (labeled 1 and 2) are for  $h_+ = 10$  km. The first curve represents the density calculated for the point discharge. The second curve represents results for a disk discharge, the disk radius being limited by

the condition that the field nowhere exceeds  $E_t$  before the discharge. The last two curves (labeled 3 and 4) represent analogous results for  $h_+ = 15$  km. We see that the runaway electron production depends strongly not only on the value of the charge lowered to the ground, but also on its altitude. For a higher location of the initial positive charge, the runaway electron flux escaping from the lower ionosphere is much higher.

The motion of electrons that constitute the runaway electron avalanche is affected by the geomagnetic field at altitudes  $>35$  km, so that the beam is not directed vertically upward, but instead moves along the geomagnetic field lines, as shown by *Lehtinen et al.* [1999]. The effect of the geomagnetic field at those altitudes is that the runaway electrons are accelerated only by the electric field component along the geomagnetic field. The accelerating field is smaller due to this fact and also because the electrons are shifted away from the region directly above the source charge to regions where the electric field is smaller. However, the path along which the electrons accelerate is now longer, because it is tilted with respect to the vertical. These two effects counteract each other. Calculations of the runaway electron density, using equation (1) and taking into account the change of the shape of electron trajectories and the decrease of the effective accelerating electric field, show that the electron density at 80 km altitude is decreased only by 30% at locations with magnetic dip angles of  $\sim 45^\circ$  (as compared to a case with a vertical geomagnetic field), which corresponds to  $30^\circ$  of magnetic latitude.

### 3. Electron distribution in the conjugate hemisphere

The energetic runaway electron beam entering the magnetosphere interacts with the background plasma during its field-aligned transport between hemispheres, depicted schematically in Figure 1. While the momentum space distribution of the runaway beam as it escapes upward has been determined by a Monte Carlo method [Lehtinen *et al.*, 1999] and has the general shape shown in Figure 4, significant modification of this distribution can occur as a result of beam-plasma interactions depending on whether the growth rate is high enough to lead to significant growth of Langmuir waves during a single traverse of the beam from its source regions to the conjugate hemisphere. If significant growth does occur, the beam loses energy to waves and is also scattered in pitch angle. If, on the other hand, the growth rate is small, then we can conclude that the beam remains largely intact during its traverse with most of the particles arriving into the conjugate hemisphere with pitch angles well below the loss cone and thus precipitating into the lower ionosphere.

In assessing this problem, Lehtinen *et al.* [2000] considered the growth rate of beam-plasma instability for the case of a relativistic beam with a significant energy spread and concluded that rapid growth of plasma waves occurs for  $N_R \geq 100 \text{ m}^{-3}$ . Since typical values for  $N_R$  are believed to be in the range  $10^4$  to  $10^5 \text{ m}^{-3}$  [Lehtinen *et al.*, 2000], very large and indeed nonlinear growth of Langmuir waves occurs, leading to intense pitch angle and energy scattering. Although, as discussed by Lehtinen *et al.* [2000], the thermalization at higher electron energies may not be completely achieved,

we assume for the purpose of the calculation of precipitating electron effects that the electrons acquire an isotropic thermal distribution (over pitch angles and energies) within a single traverse along the field line. This assumption is reasonable especially in view of the fact that the results in the conjugate hemisphere depend mostly on the typical energy of precipitating electrons and not on the details of the energy distribution. Thus, the resultant phase space distribution is taken to be the Maxwellian distribution generalized to relativistic temperatures, given by the canonical Gibbs distribution for an ideal gas:

$$f_{\text{th}}(\mathbf{r}, \mathbf{p}) \propto \exp \left[ -\frac{H(\mathbf{r}, \mathbf{p})}{k_B T} \right], \quad (4)$$

where  $H$  is the Hamiltonian of a single particle. After substitution  $H(p) = \sqrt{m^2 c^4 + p^2 c^2}$ , the distribution over kinetic energy is given by

$$f_{\text{th},\mathcal{E}}(\mathcal{E}) = C e^{-\mathcal{E}/(k_B T)} \gamma \sqrt{\gamma^2 - 1}, \quad (5)$$

where  $C$  is the normalization factor,  $\mathcal{E}$  is the kinetic energy, and  $\gamma \equiv 1 + \mathcal{E}/(mc^2)$  is the relativistic factor. The temperature for our parameters is found to be  $k_B T \simeq 2$  MeV.

With an isotropic distribution of downcoming particles incident on the conjugate hemisphere, the fraction of the particles which are precipitated can be determined as the portion of the solid angle which lies within the loss cone. The remaining electrons mirror in the conjugate hemisphere and contribute to the population of the radiation belts, eventually forming trapped electron curtains as described in [Lehtinen *et al.*, 2000].

The local pitch angle  $\alpha$  at the precipitation point is related to the equatorial pitch



angle  $\alpha_{\text{eq}}$  as

$$\frac{\sin \alpha}{\sin \alpha_{\text{eq}}} = \sqrt{\frac{B}{B_{\text{eq}}}} \quad (6)$$

where  $B_{\text{eq}}$  and  $B$  are respectively the Earth's magnetic field at the geomagnetic equator, and at the precipitation point. For a simple dipole model of the Earth's geomagnetic field we have

$$\frac{B}{B_{\text{eq}}} = \frac{\sqrt{1 + 3 \sin^2 \lambda}}{\cos^6 \lambda}$$

where  $\lambda$  is the geomagnetic latitude.

The equatorial loss-cone angle is  $\alpha_{\text{eq}}^{\text{lc}} = \sin^{-1} \left[ \sqrt{B_{\text{eq}}/B} \right]$ , and assuming an isotropic distribution of electrons at the equator, the fraction of electrons that precipitate in the conjugate region is thus given by

$$\frac{N_{\text{lc}}^{\text{tot}}}{N_{\text{tot}}} = \frac{1}{4\pi} \int_{\alpha_{\text{eq}}=0}^{\alpha_{\text{eq}}=\alpha_{\text{eq}}^{\text{lc}}} d\Omega_{\text{eq}} = \frac{1 - \cos \alpha_{\text{eq}}^{\text{lc}}}{2} = \frac{1}{2} \left( 1 - \sqrt{1 - \frac{B_{\text{eq}}}{B}} \right), \quad (7)$$

where  $N_{\text{lc}}^{\text{tot}}$  and  $N_{\text{tot}}$  are correspondingly the number of electrons in the loss cone and the total number of electrons. For a geomagnetic latitude of  $\sim 30^\circ$  we find from equation (7) that  $\sim 10\%$  of the total number of electrons in the beam are precipitated.

Let us assume that as observed at the geomagnetic equator, the total number of electrons in the beam (integrated over volume) with velocity per unit solid angle is  $F_{\text{eq}}(\alpha_{\text{eq}})$ . When the beam travels along the field line to the precipitation point, its angular distribution changes to another function  $F(\alpha)$ , which is determined from the conservation of the number of particles:

$$F(\alpha) = F_{\text{eq}}(\alpha_{\text{eq}}) \frac{\sin \alpha_{\text{eq}} d\alpha_{\text{eq}}}{\sin \alpha d\alpha}$$

and the pitch angles are related by (6). From this equation, we find

$$F(\alpha) = \frac{N^{\text{tot}} B_{\text{eq}}}{4\pi B} \frac{\cos \alpha}{\sqrt{1 - \frac{B_{\text{eq}}}{B} \sin^2 \alpha}}, \quad (8)$$

where  $\alpha$  lies in the range  $[0, \pi/2]$  because we only consider downgoing electrons.

#### 4. Effects in the conjugate hemisphere

With the energy and pitch angle distribution of the downgoing electron given respectively by (5) and (8), we now proceed to calculate the resultant effects (optical emissions, secondary ionization and  $\gamma$ -rays) in the conjugate hemisphere by assuming an initial beam density of  $10^5 \text{ m}^{-3}$ , a beam radius of  $\sim 10 \text{ km}$ , and a process duration of  $\sim 1 \text{ ms}$  [Lehtinen *et al.*, 1997]. Note that the beam duration is of the same order as that in the source hemisphere, since the velocity dispersion of the relativistic particles during a single interhemispheric traverse is negligible. The beam density of  $10^5 \text{ m}^{-3}$  represents the highest value consistent with observed terrestrial gamma ray flux intensities [Lehtinen *et al.*, 1997; Fishman *et al.*, 1994], with the duration of  $\sim 1 \text{ ms}$  determined by the kinematics of the beam formation process [Lehtinen *et al.*, 1997; 1999] and confirmed by the terrestrial gamma ray flash observations. The beam radius of  $\sim 10 \text{ km}$  is largely defined by the spatial configuration of the quasi-static field that drives the beam and is consistent with two-dimensional simulations of this process [Lehtinen *et al.*, 1997; 1999]. From Figure 3, it is clear that a beam density  $N_R \simeq 10^5 \text{ m}^{-3}$  would only occur in response to the removal of 500 C of charge from 15 km altitude or  $\sim 800 \text{ C}$  of charge from 10 km altitude (the latter not shown in Figure 3). The various effects

in the conjugate hemisphere are directly proportional to the numerical value of  $N_R$ . However, as we note in the context of the discussion of the different physical effects, even  $N_R = 10^3 \text{ m}^{-3}$  would lead to detectable optical and gamma ray emissions, while still being consistent with the CGRO observations of terrestrial gamma ray flux levels in the parent hemisphere.

In our calculations below and based on the above discussion, we assume that 10% of the beam electrons are precipitated, i.e., the density of the precipitating beam is  $N_{\text{precip}} = 10^4 \text{ m}^{-3}$  and the total number of precipitating electrons (contained within the beam of 10 km radius) for  $N_R = 10^5 \text{ m}^{-3}$  is  $N_{\text{precip}}^{\text{tot}} = 3 \times 10^{17}$ . For reference purposes, the value  $N_{\text{precip}} = 10^4 \text{ m}^{-3}$  and the assumed thermal energy distribution correspond to a precipitation flux for  $>1 \text{ MeV}$  electrons of  $\sim 3 \times 10^8 \text{ cm}^{-2}\text{-s}^{-1}$ .

We now proceed to use a Monte Carlo method to simulate the interaction of the precipitating energetic electrons with the neutral atmosphere and determine the resultant optical emissions, secondary ionization and  $\gamma$ -rays. In addition to the processes described in [Lehtinen *et al.*, 1999] for the propagation of energetic electrons in the atmosphere, we also include the magnetic mirroring effect.

We start our Monte Carlo calculations at an altitude of 200 km, with random initial electron momenta satisfying a thermal energy distribution given in (5) and angular distribution given in (8). We specify the initial energy  $\mathcal{E}$  for a precipitating particle by the use of the cumulative distribution function  $X_{\mathcal{E}}(\mathcal{E})$  defined as

$$X_{\mathcal{E}}(\mathcal{E}) \equiv \frac{\int_0^{\mathcal{E}} f_{\mathcal{E}}^{\text{th}}(\mathcal{E}) d\mathcal{E}}{\int_0^{\infty} f_{\mathcal{E}}^{\text{th}}(\mathcal{E}) d\mathcal{E}}$$

and the fact that the random variable  $X_{\mathcal{E}}$  is uniformly distributed in the interval  $[0, 1]$ . The equation  $X_{\mathcal{E}}(\mathcal{E}) = X_{\mathcal{E}}$  is solved numerically for a randomly chosen  $X_{\mathcal{E}}$  to find the energy  $\mathcal{E}$ .

The random pitch angle of a downcoming particle is specified by inverting the cumulative distribution function  $X_{\alpha}(\alpha)$  defined as:

$$X_{\alpha}(\alpha) \equiv \int_0^{\alpha} \frac{F(\alpha')}{N_{lc}^{tot}} 2\pi \sin \alpha' d\alpha' = \frac{1 - \cos \alpha_{eq}}{1 - \cos \alpha_{eq}^{lc}}$$

The random variable  $X_{\alpha}$  is uniformly distributed in the interval  $[0, 1]$ . The random pitch angle is obtained in terms of  $X_{\alpha}$  as

$$\alpha = \sin^{-1} \left[ \sqrt{\frac{B}{B_{eq}} \left\{ 1 - \left[ 1 - X_{\alpha} \left( 1 - \sqrt{1 - \frac{B_{eq}}{B}} \right) \right]^2 \right\}} \right]$$

The Monte Carlo method allows us to accurately estimate the evolution of the electron distribution function which in turn is used to estimate the optical emissions, ionization and  $\gamma$ -rays. Most of the downcoming electrons are deposited, although a small fraction ( $\sim 12\%$ ) are found to be backscattered. The backscattered electrons are in the loss cone and by the very fact that they are already near or below the mirror altitude also precipitate after several bounces.

#### 4.1. Optical emissions

We calculate the optical emissions of molecular bands using a steady-state solution for excited state populations, similar to that utilized and described by *Bell et al.* [1995]. The steady-state solution can be used because the lifetimes of the levels (less than several  $\mu s$  [*Vallance Jones*, 1974, p. 119]) are small compared to the characteristic time

scale of the change in the relativistic electron distribution  $\sim 1$  ms for our problem, as indicated by the terrestrial  $\gamma$ -ray flashes [*Fishman et al.*, 1994]. We consider the optical emission in band groups listed in Table 1. For brevity, we will call the levels only by their Latin letters, e.g., First Positive N<sub>2</sub> group is due to transition  $B \rightarrow A$ .

The emission intensities for the so-called *forbidden* “auroral” lines of atomic oxygen [*Rees*, 1989, p. 177], namely the red line (doublet) at 6300 Å and 6363 Å, due to the “forbidden” transition  $O(^1D_2) \rightarrow O(^3P_{2,1})$  and the green line at 5577 Å, due to the “forbidden” transition  $O(^1S_0) \rightarrow O(^1D_2)$ , can be calculated by solving the time-evolution equations for excited state populations. However, due to the fact that the time scale of the atomic oxygen forbidden radiation transitions ( $\gtrsim 1$  s [*Chamberlain*, 1961, p. 580]) is much longer than the beam duration scale ( $\sim 1$  ms), the emissions due to these lines are in our case negligible compared to those of the molecular bands.

The electronic (optical) level excitation rates are calculated differently for neutral and ionized molecules, as described below, and also in a manner similar to the method used by *Bell et al.* [1995]. The excitation rate  $R_\alpha^k$ , defined as the number of molecules of species  $\alpha$  in excited state  $k$  produced in unit time per unit volume, is given by

$$R_\alpha^k = N_\alpha \int_0^\infty v f_\mathcal{E}(\mathcal{E}) \sigma_\alpha^k(\mathcal{E}) d\mathcal{E}. \quad (9)$$

In this equation,  $N_\alpha$  is the density of unexcited molecules,  $\sigma_\alpha^k(\mathcal{E})$  is the optical level excitation cross-section which depends on the energy of the colliding electron  $\mathcal{E}$ ,  $v$  is the colliding electron velocity, corresponding to energy  $\mathcal{E}$ , and  $f_\mathcal{E}(\mathcal{E})$  is the electron energy distribution function. The distribution function  $f_\mathcal{E}(\mathcal{E})$  is defined so that  $f_\mathcal{E}(\mathcal{E})\Delta\mathcal{E}$  gives

the number of electrons in energy range  $[\mathcal{E}, \mathcal{E} + \Delta\mathcal{E}]$  in a unit volume.

For neutral molecules, it is known that the cross-sections  $\sigma_\alpha^k(\mathcal{E})$  have a maximum at low electron energy  $\mathcal{E}_\alpha^k$ , of the order of  $\sim 10\text{--}100$  eV, and a shape width  $\Delta\mathcal{E}_\alpha^k$  of the same order. We therefore can write approximately

$$R_\alpha^k \simeq N_\alpha v(\mathcal{E}_\alpha^k) f_\mathcal{E}(\mathcal{E}_\alpha^k) [\sigma_\alpha^k]_{\max} \Delta\mathcal{E}_\alpha^k, \quad (10)$$

where  $[\sigma_\alpha^k]_{\max} \simeq \sigma_\alpha^k(\mathcal{E}_\alpha^k)$  is the maximum value of the cross-section, and the product  $f_\mathcal{E}(\mathcal{E}_\alpha^k) \Delta\mathcal{E}_\alpha^k$  can be interpreted as the number density of the relevant excitation-producing electrons. We must note that this analysis is very approximate. For a more precise analysis, the electron distribution must be found for electron energies  $\lesssim 100$  eV, i.e., by means of solving a kinetic equation, well beyond the scope of the current work. The tail of electron distribution (with energy  $\gtrsim 100$  eV) would play an indirect role in excitation by producing new electrons which excite the molecules. We do not consider the effect of electrons with energy in the interval  $\sim 100 \text{ eV} < \mathcal{E} < \mathcal{E}_{\min}$ , where  $\mathcal{E}_{\min} = 2$  keV is the lower boundary of electron energies in Monte Carlo calculations.

The Monte Carlo model used in this work, designed specifically for energetic electrons, does not allow calculation of the electron distribution at energies less than the threshold  $\mathcal{E}_{\min} = 2$  keV. Therefore, we can estimate the value of  $f_\mathcal{E}(\mathcal{E}_\alpha^k)$  only indirectly by calculating the ionization produced by electrons with  $\mathcal{E} > \mathcal{E}_{\min}$  which have the known Monte Carlo distribution function  $f_\mathcal{E}^{\text{MC}}(\mathcal{E})$ . We have

$$f_\mathcal{E}(\mathcal{E})|_{\mathcal{E} < \mathcal{E}_{\min}} \simeq T(\mathcal{E}) \sum_\beta N_\beta \int_{\mathcal{E}_{\min}}^{\infty} v' \sigma_\beta^{\text{ion}}(\mathcal{E}', \mathcal{E}) f_{\mathcal{E}'}^{\text{MC}}(\mathcal{E}') d\mathcal{E}' \quad (11)$$

where  $T(\mathcal{E})$  is the average lifetime of electron of energy  $\mathcal{E}$  before thermalization,

$\sigma_{\beta}^{\text{ion}}(\mathcal{E}', \mathcal{E})$  is the differential ionization cross-section for species  $\beta$  as a function of the primary ( $\mathcal{E}'$ ) and secondary ( $\mathcal{E}$ ) electron energies,  $v'$  is the velocity of primary electrons, and the summation is over all atmospheric species  $\beta$ . In this estimate, we neglect the ionization process in which the electrons of energy  $\mathcal{E}$  are created by electrons with small energies  $\mathcal{E}' < \mathcal{E}_{\text{min}}$ . In the middle atmosphere, with nitrogen and oxygen being the dominant species, we can use the average ionization cross-section  $\sigma_m^{\text{ion}} \simeq 0.2\sigma_{\text{O}_2}^{\text{ion}} + 0.8\sigma_{\text{N}_2}^{\text{ion}}$  and molecular density  $N_m = N_{\text{O}_2} + N_{\text{N}_2}$ , and avoid summation in equation (11).

The lifetime of electrons is given by

$$T(\mathcal{E}) = \frac{S(\mathcal{E})}{v} \quad (12)$$

where

$$[S(\mathcal{E})]_{\text{m}} = \frac{8.93 \times 10^{19} + 1.11 \times 10^{21}([\mathcal{E}]_{\text{keV}})^{1.67}}{[N_m]_{\text{m}^{-3}}}, \quad (13)$$

is the electron range, defined as the distance that an electron with initial energy  $\mathcal{E}$  traverses before it thermalizes, and  $v$  is the electron velocity. The electron range expression is taken from *Rees* [1989, p. 40]. For the values of  $\mathcal{E}$  which are relevant for optical excitations we can neglect the energy-dependent term.

The integration in equation (11) is performed over the distribution obtained in the course of the Monte Carlo calculation, given by

$$f_{\mathcal{E}}^{\text{MC}}(\mathcal{E}) = K \sum_{i=1}^{N_s} w_i \delta(\mathcal{E} - \mathcal{E}_i) \quad (14)$$

with the sum of Dirac  $\delta$ -functions taken over  $N_s$  quasi-particles with weights  $w_i$  and energies  $\mathcal{E}_i$ , and where  $K$  is the normalization coefficient determined by the fact that

$K \sum w_i$  must be equal to the number density of energetic electrons. The presence of the  $\delta$ -functions converts the integral of the form  $\int f_{\mathcal{E}}^{\text{MC}}(\mathcal{E})G(\mathcal{E})d\mathcal{E}$  with  $G(\mathcal{E})$  being an arbitrary function of  $\mathcal{E}$  to a sum over quasiparticles  $K \sum w_i G(\mathcal{E}_i)$ .

Using equations (10) through (14), we find the excitation rate for the optical level  $k$  to be

$$R_{\alpha}^k \simeq 8.93 \times 10^{19} \times K N_{\alpha} [\sigma_{\alpha}^k]_{\text{max}} \Delta \mathcal{E}_{\alpha}^k \sum_{i=1}^{N_s} w_i v_i \sigma_m^{\text{ion}}(\mathcal{E}_i, \mathcal{E}_{\alpha}^k). \quad (15)$$

In calculations of optical emissions in the stratified atmosphere, we also take into account the fact that the emissions come from different altitudes with different atmosphere densities.

The excitation rates of ionized states are calculated in a different, but somewhat analogous manner. Since the ambient ionization in the atmosphere is very small, the excitation of molecular ions is not an important process. Instead, the ionization by electron impact leads to the production of ions already in the excited states. According to *Van Zyl and Pendleton [1995]*, the creation of  $\text{N}_2^+$  has branching ratios  $p^A = 53.5\%$  and  $p^B = 14.5\%$ , for levels  $A$  and  $B$ , respectively (measured for 100-eV electrons), and the creation of  $\text{O}_2^+$  has  $p^b = 15\%$  for level  $b$ . Aside from the need to take into account the branching ratio  $p$ , excitation rate  $R_{\alpha}^k$  for the ionized states is given by an expression similar to (9), except for the fact that  $\sigma_{\alpha}^k(\mathcal{E})$  should be replaced by the total cross-section  $[\sigma_{\alpha}^{\text{ion}}]^{\text{tot}}(\mathcal{E})$  for ionization by an electron with initial energy  $\mathcal{E}$ :

$$[\sigma_{\alpha}^{\text{ion}}]^{\text{tot}}(\mathcal{E}) = \int_0^{\mathcal{E}-I_{\alpha}} \sigma_{\alpha}^{\text{ion}}(\mathcal{E}, \mathcal{E}') d\mathcal{E}', \quad (16)$$

where  $\mathcal{E}'$  is the energy of the secondary electron,  $I_{\alpha}$  is the ionization potential, and the



integration is performed over the secondary electron energies  $\mathcal{E}'$ .

Following the analysis performed above and using the total ionization cross-section in place of the level excitation cross-section  $\sigma_\alpha^k(\mathcal{E})$ , we arrive at the expression for excitation rate for ions, somewhat similar to equation (15):

$$R_\alpha^k \simeq p_\alpha^k \times 8.93 \times 10^{19} \times K N_\alpha [\sigma_\alpha^{\text{ion}}]_{\text{max}}^{\text{tot}} \Delta \mathcal{E}_\alpha^{\text{ion}} \sum_{i=1}^{N_s} w_i v_i \sigma_m^{\text{ion}}(\mathcal{E}_i, \mathcal{E}_\alpha^{\text{ion}}) \quad (17)$$

where  $N_\alpha$  is the non-ionized species density,  $\sigma_{\alpha, \text{max}}^{\text{ion, tot}}$  is the maximum of the ionization cross-section, and  $\Delta \mathcal{E}_\alpha^{\text{ion}}$  is the width of the total ionization cross-section curve.

The ionization cross-section of species  $\alpha$  for the purposes of this work was fitted with expression analogous to *Rees* [1989, p. 43]:

$$\sigma_\alpha^{\text{ion}}(\mathcal{E}, \mathcal{E}') \simeq \frac{2\pi r_0^2 Z_\alpha}{v^2 (\mathcal{E}_{i\alpha} + \mathcal{E}')^2} \quad (18)$$

where  $r_0$  is the classical electron radius,  $Z_\alpha$  is the molecular nuclear charge,  $\mathcal{E}$ ,  $\mathcal{E}'$  are respectively the energies of primary and secondary electrons,  $v$  is the velocity of the primary electron and  $\mathcal{E}_{i\alpha}$  is the typical ionization energy. For main molecular species we have  $\mathcal{E}_{iN_2} = 13.0$  eV,  $I_{N_2} = 15.6$  eV,  $Z_{N_2} = 14$ ,  $\mathcal{E}_{iO_2} = 17.4$  eV,  $I_{O_2} = 12.2$  eV,  $Z_{O_2} = 16$ . The values of  $\mathcal{E}_\alpha^k$ ,  $\sigma_{\alpha, \text{max}}^k$ ,  $\Delta \mathcal{E}_\alpha^k$  for relevant species are given in Appendix A.

The volume emission rates  $\varepsilon_\alpha^b$  of species  $\alpha$  in the band  $b$  are obtained from the excitation rates as a solution of a steady-state level population equation, because the level lifetimes are small compared to the characteristic time scale of 1 ms relevant for our problem. The expressions used are given in Appendix B.

The calculated altitude profiles for the five molecular bands enumerated in Table 1 are presented in Figure 5. The precipitating electron flux was taken to have a density

of  $N_{\text{precip}} \simeq 10^4 \text{ m}^{-3}$  (the flux of  $F_{>1 \text{ MeV}} \simeq 3 \times 10^8 \text{ el-cm}^{-2}\text{-s}^{-1}$ ), lasting for 1 ms, corresponding to the initial runaway electron density of  $N_R = 10^5 \text{ m}^{-3}$ . The Figure 5a presents the altitude and time dependence of the photon production rate in the first positive band of  $\text{N}_2$ . Figure 5b presents the time-integrated optical emission intensities in the five molecular bands, converted to Rayleigh-seconds. The optical emission intensity in Rayleighs is given by [*Chamberlain*, 1961, p. 569]:

$$I = 10^{-10} \int \varepsilon dl \simeq \varepsilon d,$$

where the integration is along the line of sight,  $\varepsilon$  is the volume emission rate in  $\text{ph-m}^{-3}\text{-s}^{-1}$ , and  $d \simeq 2 \times 10^4 \text{ m}$  is the transverse size of the beam.

The optical emission intensities shown in Figure 5 are easily detectable by standard imaging and photometric instruments in terms of brightness levels. However, the emissions last only for a few ms, so that high frame rate photometric imaging would be needed. Also, the transverse extent of the beam is only  $\sim 20 \text{ km}$ , so that accurate pointing or very wide aperture (e.g., all-sky cameras) instruments would need to be used. For example, peak intensity of  $\sim 10^3 \text{ R-s}$  for  $\text{N}_2$  1P band, lasting for 1 ms, corresponds to  $\sim 1 \text{ MR}$ , comparable to the peak intensities of transient optical flashes known as elves [see Figure 2 of *Inan et al.*, 1997]. These brief optical pulses can be detected with sensitive photodetectors even if their peak intensities were lower by one or two orders of magnitude.

The optical emissions produced by the precipitating component of the relativistic electron beam which is caused by a lightning flash in the conjugate hemisphere may

be loosely termed to be “conjugate sprites”, to be distinguished from sprites produced in the hemisphere of the causative flash by quasi-electrostatic heating of ambient electrons. It is interesting to note that the dominant emissions are in the blue  $N_2^+$  1N and  $N_2$  2P bands, and in the red  $N_2$  1P band, as shown in Figure 5b, so that these “conjugate sprites” are not predominantly red as their counterparts produced overhead thunderstorms [Mende *et al.*, 1995]. The combination of the red and blue colors would lead to a sprite which exhibits purple color. For ground-based observations of the optical emissions one should also take into account the relatively greater attenuation of blue light as compared with red light in the atmosphere due to Rayleigh scattering. Note that the transverse structure of the runaway electron beam in the parent hemisphere is basically determined by the smooth spatial variation of the quasi-static field and does not exhibit fine structure. Accordingly, the conjugate sprites are expected to be amorphous glows of  $\sim 20$  km transverse extent.

The optical emissions from the energetic electrons in the conjugate sprites are detectable, unlike the emissions produced by runaway electrons in the red sprites occurring above thunderstorms [Lehtinen *et al.*, 1999], although 90% of the energetic electrons are lost in the magnetosphere. The apparent disagreement is in fact physically reasonable and is due to two causes: (1) the downgoing electrons interact with a thick (increasing density) target and deposit all of their energy, in contrast to the upgoing electrons which interact with a thin (decreasing density) target, primarily because the upgoing electron avalanche grows to appreciable magnitude only at high altitudes; (2) the optical emission intensity from the runaway electrons above the thunderstorm is

lower than that from the ambient free electrons heated by the presence of quasi-static electric field. These relatively weak emissions cannot be observed in the presence of the much larger optical emissions from the heated ambient electrons. In the conjugate hemisphere, on the other hand, there is no heating of the ambient electrons to mask the emissions due to the energetic electrons.

To further illustrate and quantify the first point, Figure 6, shows a comparison of the energy deposition by the upgoing runaway electron beam and precipitating electrons. The precipitating beam is assumed to have lost 90% of its energy in the magnetosphere. Despite this, the total energies deposited in both cases are the same, demonstrating a greater efficiency of energy deposition by the downgoing beam.

The observations of optical emissions with properties similar to those expected may have been made in the past, in the form of the so-called *fast atmospheric pulsations* [Ögelman, 1973]. The events observed by Ögelman [1973] have a typical time scale of 1 ms, have emissions within 4300 to 6300 Å spectral range, sometimes ( $\lesssim 5\%$  cases) have a horizontal extent of up to 175 km, but they are never so broad as to be caused by astrophysical phenomena. Some such events are associated with lightning [Winckler *et al.*, 1993] and can be interpreted as red sprites and elves [transient optical emissions, see, e.g. Inan *et al.*, 1997]. However, other similar events are not associated with lightning [Nemzek and Winckler, 1989], suggesting that they may be caused by precipitation of electrons of  $\sim 2$  MeV energy [LaBelle, 1988]. The source considered by LaBelle [1988] was the radiation-belt electrons scattered by lightning-induced waves in the magnetosphere and was criticized by Vampola [1988] on the basis of the fact that

the energetic electron flux in the inner belt was too low to cause the observed optical emissions. This critique does not apply to the precipitating runaway electrons in the hemisphere conjugate to lightning since they are supplied by an external source. At the same time, *Ögelman* [1973] observed a clear 10 kHz modulation in most events, which is not inherent in any aspect of the runaway electron beam processes discussed here. It thus remains to be seen whether fast atmospheric pulsations are indeed conjugate signatures of the runaway breakdown.

## 4.2. Secondary ionization

The secondary electron production rate is calculated directly from the energy deposition rate by assuming that every deposited 35 eV energy creates an electron-ion pair [Rees, 1963]. The time dependence of electron density  $N_e$  due to chemical reactions in the atmosphere is calculated using the model of *Glukhov et al.* [1992]. This model accounts for the dynamics of three other charged atmospheric constituents, namely the density of positive and negative ions and positive cluster ions, and takes into account the temperature dependence of the various reaction rate coefficients. We make the following corrections to the coefficients of equations (1) through (4) of *Glukhov et al.* [1992]. The effective coefficient of dissociative recombination (denoted  $\alpha_d$  by *Glukhov et al.* [1992]) is taken to be equal to  $6 \times 10^{-7} \text{ cm}^3 \text{ s}^{-1}$ , according to the value in [Rodriguez and Inan, 1994], and the effective electron detachment rate (denoted  $\gamma$  by *Glukhov et al.* [1992]) is  $3 \times 10^{-18} N_m \text{ s}^{-1}$ , where  $N_m$  is the total density of neutrals, according to *Pasko and Inan* [1994]. The value of the effective electron detachment rate is estimated

by *Glukhov et al.* [1992] using the ratio  $N_0^-/N_{e0}$  of the ambient negative ion and electron densities. The experimentally measured value, quoted by *Glukhov et al.* [1992] is  $N_0^-/N_{e0} \sim 1$  at the altitude of  $\sim 80$  km, which gives the effective electron detachment rate of  $3 \times 10^{-17} N_m \text{ s}^{-1}$ . Neglecting this coefficient altogether would give  $N_0^-/N_{e0} \simeq 10^2$  at altitude  $\sim 80$  km, which is greater by two orders of magnitude. The value  $N_0^-/N_{e0} = 1$  in the case of no electron detachment is attained at  $\sim 92$  km.

Knowing the change in electron density, we can estimate the change of ionosphere conductivity at different altitudes. The total conductivity is  $\sigma_0 = \sigma_i + \sigma_e$ , where  $\sigma_i$  is the ambient ion conductivity and  $\sigma_e$  is the electron conductivity which is changed by the precipitation. The ion conductivity is derived from total ambient conductivity in [*Hale, 1994*] by subtracting the electron part. For electrons, we have  $\sigma_e = q_e N_e \mu$ , where  $\mu = 3.66 \times 10^{25}/N_m$  is the electron mobility [*Davies, 1983*], with  $N_m$  in  $\text{m}^{-3}$  and  $\mu$  in  $\text{m}^2\text{-V}^{-1}\text{-s}^{-1}$ .

The initial ionization enhancement and conductivity are plotted in Figure 7, and the calculated time dependence of the electron density at altitudes of 70 and 80 km is plotted in Figure 8. The electron density and associated conductivity changes shown in Figure 7 are detectable by means of subionospheric VLF remote sensing, in spite of the relatively small  $\sim 20$  km lateral extent of the ionospheric disturbance. As a crude assessment of this detectability, we consider equation (1) of *Inan et al.* [1985], according to which the phase change  $\Delta\phi$  of a 20 kHz subionospheric signal due to a reflection height change  $\Delta h$  over a length  $d$  of a long ( $>2000$  km) VLF propagation path is given

by

$$[\Delta\phi]_{\text{deg}} \simeq -0.0034 [d]_{\text{km}} [\Delta h]_{\text{km}}, \quad (19)$$

where we have assumed an ambient (unperturbed) VLF reflection height of  $\sim 85$  km. To determine  $\Delta h$  corresponding to the modified electron density profile given in Figure 7a, we can consider the fact that VLF reflection typically occurs when  $(\omega_p^2/\nu) \simeq 2.5 \times 10^5 \text{ s}^{-1}$ , where  $\omega_p$  and  $\nu$  are respectively the local plasma and effective electron collision frequency. Applying this criterion on the ambient and disturbed profiles of Figure 7a, we find the ambient reflection height to be  $\sim 85$  km, and  $\Delta h \simeq -2.5$  km. Using this value and  $d \simeq 20$  km in (19) we find  $\Delta\phi \simeq 0.17^\circ$ , which is detectable [Wolf and Inan, 1990].

Equation (19) is in fact only valid for relatively small perturbations near the VLF nighttime reflection height of  $\sim 85$  km [Inan *et al.*, 1985]. It is clear from Figure 7 that the conductivity changes produced by the precipitating energetic electrons are large (i.e.,  $\Delta N \gg N_{e0}$ ) and occur over a very broad range of altitudes. The range of VLF amplitude and phase changes that would be produced by such a disturbance was estimated using the Long Wave Propagation Capability (LWPC) code which is available at Stanford and which has in the past been used to quantify VLF signatures of lightning-induced electron precipitation bursts [Lev-Tov *et al.*, 1996, and references therein]. Calculations indicate that the sudden appearance of a disturbance of lateral extent  $\sim 20$  km and with a disturbed conductivity profile as given in Figure 7b on a relatively long (a few thousand km) subionospheric path leads to amplitude changes of several dB and phase changes of several degrees, depending on the location of the

receiver. These types of amplitude and phase changes are easily detectable, being well above the typical lowest detectable signal changes of  $\sim 0.1$  dB in amplitude and  $\sim 0.5^\circ$  in phase [Wolf and Inan, 1990]. To the authors' knowledge, however, so far there has been no reliable observation of a VLF signal perturbation which would occur at a position outside a storm, but which would map geomagnetically to a storm in the opposite hemisphere.

### 4.3. $\gamma$ -ray Emissions

Energetic precipitating electrons produce  $\gamma$ -rays through the process of bremsstrahlung, with the photons being emitted by the downward going relativistic electrons predominantly in the forward direction. The downward moving photons cannot penetrate the full depth of the atmosphere, and are not detectable on the ground, but are strongly scattered by the increasingly dense atmosphere which constitutes an optically 'thick' target. The scattered photons which move upward can be detected by a satellite. This circumstance is different from that considered by *Lehtinen et al.* [1997], who studied the case of  $\gamma$ -rays emitted at  $\sim 60$ – $70$  km altitude and in the upward direction toward an increasingly tenuous (i.e., 'thin' target) atmosphere so that the photon transport to satellite altitudes was straightforward. For the case in hand, we need to consider multiple scattering of the  $\gamma$ -ray photons and use a Monte Carlo model of  $\gamma$ -ray propagation, such as employed by *Inan et al.* [1999] in considering the ionospheric effects of a gamma ray flare originating in a distant magnetar.

The processes which mostly determine the photon propagation are the Compton



scattering and photoeffect. The results of the Monte Carlo simulation are presented in Figure 9. The predicted spectrum is hard for photon energies  $\mathcal{E}_{\text{ph}} < 100$  keV and soft for  $\mathcal{E}_{\text{ph}} > 100$  keV, as a result of low-energy photons being attenuated due to photoeffect. The maximum photon flux (in the range  $\mathcal{E}_{\text{ph}} > 5$  keV) at the satellite altitude for our value of precipitating electron density ( $N_{\text{precip}} = 10^4 \text{ m}^{-3}$ , which corresponds to energy flux of  $\sim 10^3 \text{ erg-cm}^{-2}\text{-s}^{-1}$ , precipitating over area of  $100 \text{ km}^2$ ) is  $\sim 10^8 \text{ ph-m}^{-2}\text{-s}^{-1}$ . The fractional distribution of these photons in the energy ranges of the BATSE instrument on the CGRO satellite [Fishman *et al.*, 1994] is as follows:  $\sim 24\%$  in the 20–50 keV,  $\sim 36\%$  in the 50–100 keV,  $\sim 31\%$  in the 100–300 keV,  $\sim 8\%$  in the  $> 300$  keV energy range. The minimum flux detectable by BATSE (i.e., a single count in a 0.1 ms time interval) in any of these energy ranges is  $\sim 2 \times 10^4 \text{ ph-m}^{-2}\text{-s}^{-1}$ , while the data in Figure 9c,d correspond to  $\sim 2500$  counts in 0.1 ms, or a flux of  $5 \times 10^7 \text{ ph-m}^{-2}\text{-s}^{-1}$  in 100–300 keV energy range. Even if the beam density were lower by two orders of magnitude, i.e.  $N_R \simeq 10^3 \text{ m}^{-3}$ , the gamma ray fluxes produced in the conjugate hemisphere would be  $5 \times 10^5 \text{ ph-m}^{-2}\text{-s}^{-1}$  (or 25 counts in 0.1 ms), detectable by BATSE.

*Lehtinen et al.* [1999] calculated a maximum photon flux of 200 counts in 0.1 ms in the 100–300 keV energy range, produced in the hemisphere of the causative lightning by an upgoing runaway electron beam of density  $N_R \simeq 10^3 \text{ m}^{-3}$  and 100 km width, produced by the linearly extended charge configuration used in that paper. For the case of a point discharge, a narrow beam of  $\sim 10$  km width with density  $N_R \simeq 10^5 \text{ m}^{-3}$  would give  $\sim 2000$  counts, corresponding approximately to the same value as obtained by *Lehtinen et al.* [1997].

A value of  $\sim 2000$  counts on 0.1 ms in the 100-300 keV energy range is similar to the value of  $\sim 2500$  counts estimated above for the emissions in the conjugate hemisphere produced by the runaway electron beam of initial density  $N_R \simeq 10^5 \text{ m}^{-3}$ , although  $\sim 90\%$  of the initial beam is lost in the magnetosphere. The emissions in the conjugate hemisphere, however, are smaller than those predicted to exist above a thunderstorm in the lowest BATSE energy range of 20–50 keV, due to the spectral differences. The radial structure of the photon flux at the satellite altitude, plotted in Figure 9c shows that the upgoing photon beam produced by the precipitating electrons in the conjugate hemisphere is broader than the one produced by the upgoing runaway beam [Figure 9a in *Lehtinen et al.*, 1999]. The total energy depositions in the form of bremsstrahlung are of the same order of magnitude in these two cases (see Figure 6), although the downgoing beam energy is only  $\sim 10\%$  of the initial runaway beam energy. The more effective emission of photons is due to the fact that downgoing electrons deposit all of their energy in the atmosphere which essentially constitutes a thick target while the upgoing ones interact with atmosphere at high altitudes, where it is a thin target. Once again, we note that even if the initial beam density were lower by two orders of magnitude, i.e.  $N_R \simeq 10^3 \text{ m}^{-3}$ , the gamma ray fluxes produced in the conjugate hemisphere would be  $5 \times 10^5 \text{ ph-m}^{-2}\text{-s}^{-1}$  (or 25 counts in 0.1 ms), detectable by BATSE.

#### 4.4. Accuracy of Calculations

The Monte Carlo model of downgoing electron beam used  $\sim 2 \times 10^4$  quasi-particles, which would give a statistical error of less than one percent for the total initial ionization,

and of a few percent at its peak value. The number of gamma photons used to obtain the data in Figure 9 is  $\sim 1.1 \times 10^4$ . The error in the spectrum, Figure 9b, is estimated to be of the order of 3% at the maximum value. In respect to optical emissions, the largest error is due to the simplified model used to obtain them, and can be of the order of tens of percent. The same applies to the calculations of the phase change of the VLF wave.

## 5. Conclusions

We considered the fate of energetic runaway electron beams after they escape upward from the hemisphere in which they are produced via avalanche acceleration driven by intense quasi-static fields released by large positive lightning discharges. Although the beam is largely thermalized and isotropized [Lehtinen *et al.*, 2000] during its traverse between hemispheres, the particle flux which arrives in the conjugate hemisphere below the loss cone precipitates into the atmosphere, producing optical emissions, secondary ionization and gamma rays.

Monte Carlo modeling of the interaction of the downcoming beam with the atmosphere indicates that for typical beam current densities (calibrated by measured intensities of bremsstrahlung gamma rays) emissions in different optical bands, including the first and second positive bands of molecular nitrogen, and the first negative band of  $N_2^+$  are excited at levels of several tens to up to several hundred kR, detectable with properly pointed instruments having sufficient time resolution. In this context, it is important to note that the temporal duration of the emissions is  $\sim 1$  ms, and that the

lateral extent of the beam is  $\sim 20$  km. The conjugate sprites are expected to be purple in color, having roughly equal intensities of red and blue emissions.

Monte Carlo modeling further indicates that the secondary ionization produced by the precipitating energetic beam electrons is significant, leading to electron density changes of up to  $\sim 10^4$   $\text{cm}^{-3}$  over the range of altitudes of 35 to 85 km. The resultant conductivity changes are sufficiently large to produce detectable amplitude and phase changes of subionospheric VLF signals propagating underneath, in spite of the relatively small lateral extent of the secondary ionization disturbance.

The gamma ray emissions from the precipitating energetic electrons can also be detectable by the BATSE detectors on the CGRO satellite [*Fishman et al.*, 1994]. In fact, the upgoing gamma ray beam is much broader in this case than the beam produced by the upgoing electrons above the thunderstorm [*Lehtinen et al.*, 1997; 1999] and therefore can have a higher detection probability.

The downgoing electrons deposit all of their energy, in contrast to the upgoing, which just skim through the upper layers atmosphere, because the upgoing electron avalanche grows to an appreciable magnitude only at high altitudes. This explains strong optical and gamma emissions in comparison to the emissions at the origin (above a thunderstorm), although the electrons have lost 90% of their density in the magnetosphere.

Future experiments aimed at detection of the effects of the runaway electron beams in the conjugate region may provide definitive experimental evidence of the runaway acceleration mechanism, but need to be carefully conducted in view of the short duration

of the optical emissions and small lateral extent of the ionization disturbances. Also, it should be kept in mind that runaway electron beams may be produced only when unusually large quantities of charge are removed from relatively high altitude cloud tops, so that these events may be rare, requiring extended periods of observation.

### Appendix A: The values of $\mathcal{E}_\alpha^k$ , $\sigma_{\alpha,\max}^k$ , $\Delta\mathcal{E}_\alpha^k$

The relevant values for atmospheric molecular species are:

1. The First Positive Group of  $\text{N}_2$  (level  $B$ ):  $[\sigma_{\text{N}_2}^B]_{\max} = 1.1 \times 10^{-20} \text{ m}^{-2}$ ,  
 $\Delta\mathcal{E}_{\text{N}_2}^B = 10 \text{ eV}$ ,  $\mathcal{E}_{\text{N}_2}^B = 12 \text{ eV}$ .
2. The Second Positive Group of  $\text{N}_2$  (level  $C$ ):  $[\sigma_{\text{N}_2}^C]_{\max} = 3.8 \times 10^{-21} \text{ m}^{-2}$ ,  
 $\Delta\mathcal{E}_{\text{N}_2}^C = 10 \text{ eV}$ ,  $\mathcal{E}_{\text{N}_2}^C = 16 \text{ eV}$ .
3. The First Negative  $\text{N}_2^+$  group (1N) (level  $B$ ):  $[\sigma_{\text{N}_2}^{\text{ion}}]_{\max}^{\text{tot}}$  is calculated from equations (16) and (18),  $\Delta\mathcal{E}_{\text{N}_2}^{\text{ion}} \simeq 38.5 \text{ eV}$ ,  $[\mathcal{E}_{\text{N}_2}^{\text{ion}}]_{\max} \simeq 23.5 \text{ eV}$ .
4.  $\text{N}_2^+$  Meinel group (M) (level  $A$ ): see item 3.
5. The First Negative  $\text{O}_2^+$  group (1N) (level  $b$ ):  $[\sigma_{\text{O}_2}^{\text{ion}}]_{\max}^{\text{tot}}$  is calculated from equations (16) and (18),  $\Delta\mathcal{E}_{\text{O}_2}^{\text{ion}} \simeq 41 \text{ eV}$ ,  $[\mathcal{E}_{\text{O}_2}^{\text{ion}}]_{\max} \simeq 22 \text{ eV}$ .

### Appendix B: Steady-state volume emission rates

In the following equations,  $\varepsilon_\alpha^b$  is the volume emission rate of species  $\alpha$  in the band  $b$ ,  $\Lambda_\alpha^k$  is the inverse lifetime of level  $k$  (the lifetimes are given in Table 1),  $\Gamma_{\alpha,\beta}^k$  is the

quenching rate due to collisions with species  $\beta$ :

1. The First Positive Group of  $N_2$  (1P):

$$\varepsilon_{N_2}^{1P} = (R_{N_2}^B + \varepsilon_{N_2}^{2P}) \frac{\Lambda_{N_2}^B}{\Lambda_{N_2}^B + \Gamma_{N_2,air}^B (N_{N_2} + N_{O_2})}$$

Note that we take into account ‘‘cascading’’ from the higher level by the way of the emission of the Second Positive Group of  $N_2$ . The quenching rate with air is obtained by averaging the quenching rates by nitrogen and oxygen with appropriate weights,  $\Gamma_{N_2,air}^B = 0.8\Gamma_{N_2,N_2}^B + 0.2\Gamma_{N_2,O_2}^B = 5.2 \times 10^{-17} \text{ m}^3\text{s}^{-1}$ . The quenching rates  $\Gamma_{N_2,N_2}^B = 2.6 \times 10^{-17} \text{ m}^3\text{s}^{-1}$  and  $\Gamma_{N_2,O_2}^B = 1.6 \times 10^{-16} \text{ m}^3\text{s}^{-1}$  are the averages of quenching rates for different vibrational levels  $v' = 0 \dots 12$  given by *Piper* [1992], with weights corresponding to the excitation cross-sections given by *Shemansky and Broadfoot* [1971].

2. The Second Positive Group of  $N_2$  (2P):

$$\varepsilon_{N_2}^{2P} = R_{N_2}^C \frac{\Lambda_{N_2}^C}{\Lambda_{N_2}^C + \Gamma_{N_2,air}^C (N_{N_2} + N_{O_2})}$$

where the quenching rate  $\Gamma_{N_2,air}^C = 7.4 \times 10^{-17} \text{ m}^3\text{s}^{-1}$  is obtained in a manner analogous to the previous item, using the data from *Millet et al.* [1973] and *Shemansky and Broadfoot* [1971].

3. The First Negative  $N_2^+$  group (1N):

$$\varepsilon_{N_2^+}^{1N} = R_{N_2^+}^B \frac{\Lambda_{N_2^+}^B}{\Lambda_{N_2^+}^B + \Gamma_{N_2^+,air}^B (N_{N_2} + N_{O_2})}$$

where  $\Gamma_{N_2^+,air}^B = 4 \times 10^{-16} \text{ m}^3\text{s}^{-1}$  [*Vallance Jones*, 1974, p. 119].

4.  $N_2^+$  Meinel group (M):

$$\varepsilon_{N_2^+}^M = R_{A,N_2^+} \frac{\Lambda_{N_2^+}^A}{\Lambda_{N_2^+}^A + \Gamma_{N_2^+,\text{air}}^A (N_{N_2} + N_{O_2})}$$

where  $\Gamma_{N_2^+,\text{air}}^A = 7 \times 10^{-16} \text{ m}^3\text{s}^{-1}$  [*Piper et al.*, 1985].

5. The First Negative  $O_2^+$  group (1N):

$$\varepsilon_{O_2^+}^{1N} = R_{O_2^+}^b \frac{\Lambda_{N_2^+}^b}{\Lambda_{N_2^+}^b + \Gamma_{O_2^+,N_2}^b N_{N_2}}$$

where  $\Gamma_{O_2^+,N_2}^b = 2 \times 10^{-16} \text{ m}^3\text{s}^{-1}$  [*Vallance Jones*, 1974, p. 119].

**Acknowledgments.** This work was supported by NASA under grants NAGW4738 and NAG5-4554 and under NSF grant NSF-ATM-973 1170 to Stanford University. We thank M. Johnson for LWPC model calculations.

## References

- Bell, T. F., V. P. Pasko, and U. S. Inan, Runaway electrons as a source of red sprites in the mesosphere, *Geophys. Res. Lett.*, *22*, 2127, 1995.
- Burke, W. J., T. L. Aggson, N. C. Maynard, W. R. Hoegy, R. A. Hoffman, R. M. Candy, C. Liebrecht and E. Rodgers, Effects of lightning discharge detected by the DE 2 satellite over hurricane Debbie, *J. Geophys. Res.*, *97*, 6359, 1992.
- Chamberlain, J. W., *Physics of Aurora and Airglow*, Academic Press, New York, 1961.
- Davies, D. K., Measurements of swarm parameters in dry air, *Theoretical notes*, Note 346, Westinghouse R&D center, Pittsburg, May, 1983.
- Fishman, G. J., P. N. Bhat, R. Malozzi, J. M. Horack, T. Koshut, C. Kouveliotou, G. N. Pendleton, C. A. Meegan, R. B. Wilson, W. S. Paciesas, S. J. Goodman, and H. J. Christian, Discovery of intense gamma-ray flashes of atmospheric origin, *Science*, *264*, 1313, 1994.
- Franz, R. C., R. J. Nemzek, and J. R. Winckler, Television image of a large upward electric discharge above a thunderstorm system, *Science*, *249*, 48, 1990.
- Glukhov, V. S., V. P. Pasko and U. S. Inan, Relaxation or Transient Lower Ionospheric Disturbances Caused by Lightning-Whistler-Induced Electron Precipitation Bursts, *J. Geophys. Res.*, *97*, 16971, 1992.
- Gurevich, A. V., G. M. Milikh, and R. A. Roussel-Dupré, Runaway mechanism of air breakdown and preconditioning during a thunderstorm, *Phys. Lett. A*, *165*, 463, 1992.
- Hale, L. C., Coupling of ELF/ULF energy from lightning and MeV particles to the middle atmosphere, ionosphere, and global circuit, *J. Geophys. Res.*, *99*, 21089, 1994.



- Holzworth, R. H., M. C. Kelley, C. L. Siefring, L. C. Hale and J. T. Mitchell, Electrical measurements in the atmosphere and the ionosphere over an active thunderstorm. 2. Direct current electric fields and conductivity, *J. Geophys. Res.*, *90*, 9824, 1985.
- Inan, U. S., D. L. Carpenter, R. A. Helliwell and J. P. Katsufakis, Subionospheric VLF/LF phase perturbations produced by lightning-whistler induced particle precipitation, *J. Geophys. Res.*, *90*, 7457, 1985.
- Inan, U. S., S. C. Reising, G. J. Fishman and J. M. Horack, On the association of terrestrial gamma-ray bursts with lightning and implication for sprites, *Geophys. Res. Lett.*, *23*, 1017, 1996.
- Inan, U. S., C. Barrington-Leigh, S. Hansen, V. S. Glukhov, T. F. Bell, and R. Rairden, Rapid lateral expansion of optical luminosity in lightning-induced ionospheric flashes referred to as 'elves', *Geophys. Res. Lett.*, *24*, 583, 1997.
- Inan, U. S., N. G. Lehtinen, S. J. Lev-Tov, M. P. Johnson, T. F. Bell, and K. Hurley, Ionization of the lower ionosphere by  $\gamma$ -rays from a magnetar: detection of a low-energy (3–10 keV) component, *Geophys. Res. Lett.*, *26*, 3357, 1999.
- Krehbiel, P. R., R. J. Thomas, W. Rison, T. Hamlin, J. Harlin, and M. Davies, GPS-based mapping system reveals lightning inside storms, *Eos Trans. AGU*, *81*, 21, 2000.
- LaBelle, J., Are fast atmospheric pulsations optical signatures of lightning-induced electron precipitation?, *Geophys. Res. Lett.*, *15*, 279, 1988.
- Lehtinen, N. G., T. F. Bell, V. P. Pasko, and U. S. Inan, A two-dimensional model of runaway electron beams driven by quasi-electrostatic thundercloud fields, *Geophys. Res. Lett.*, *24*, 2639, 1997.

- Lehtinen, N. G., T. F. Bell, and U. S. Inan, Monte Carlo simulation of runaway MeV electron breakdown with application to red sprites and terrestrial gamma ray flashes, *J. Geophys. Res.*, *104*, 24699, 1999.
- Lehtinen, N. G., U. S. Inan, and T. F. Bell, Trapped energetic electron curtains produced by thunderstorm driven relativistic runaway electrons, *Geophys. Res. Lett.*, *27*, 1095, 2000.
- Lev-Tov, S. J., U. S. Inan, A. J. Smith, and M. A. Clilverd, Characteristics of localized ionospheric disturbances inferred from VLF measurements at two closely spaced receivers, *J. Geophys. Res.*, *101*, 15,737, 1996.
- Mende, S. B., R. L. Rairden, G. R. Swenson and W. A. Lyons, Sprite spectra; N<sub>2</sub> 1 PG band identification, *Geophys. Res. Lett.*, *22*, 2633, 1995.
- Milikh G. and J. A. Valdivia, Model of Gamma Ray Flashes due to Fractal Lightning, *Geophys. Res. Lett.*, *26*, 525, 1999.
- Millet, P., Y. Salamero, H. Brunet, J. Galy, D. Blank, and J. L. Teyssier, De-excitation of N<sub>2</sub>(C<sup>3</sup>Π<sub>u</sub>; v' = 0 and 1) levels in mixtures of oxygen and nitrogen, *J. Chem. Phys.*, *58*, 5839, 1973.
- Nemzek, R. J. and J. R. Winckler, Observation and interpretation of fast sub-visual light pulses from the night sky, *Geophys. Res. Lett.*, *16*, 1015, 1989.
- Neubert, T., T. H. Allin, H. Stenbaek-Nilsen, E. Blanc, M. Fuellekrug, G. Satori, Sprites over Europe: Results from the first European field campaign, *Eos, Trans. AGU*, *81* (48), Fall Meet. Suppl., F131, 2000
- Ögelman, H., Millisecond time scale atmospheric light pulses associated with solar and magnetospheric activity, *J. Geophys. Res.*, *78*, 3033, 1973.

- Pasko, V. P., and U. S. Inan, Recovery signatures of lightning-associated VLF perturbations as a measure of the lower ionosphere, *J. Geophys. Res.*, *99*, 17523, 1994.
- Pasko, V. P., U. S. Inan, T. F. Bell and Y. N. Taranenko, Sprites produced by quasi-electrostatic heating and ionization in the lower atmosphere, *J. Geophys. Res.*, *102*, 4529, 1997.
- Piper, L. G., Energy transfer studies on  $N_2(X^1\Sigma_g^+, V)$  and  $N_2(B^3\Pi_g)$ , *J. Chem. Phys.*, *97*, 270, 1992.
- Piper, L. G., B. D. Green, W. A. M. Blumberg and S. J. Wolnik,  $N_2^+$  Meinel band quenching, *J. Chem. Phys.*, *82*, 3139, 1985.
- Rees, M. H., Auroral ionization and excitation by incident energetic electrons, *Planet. Space Sci.*, *11*, 1209, 1963.
- Rees, M. H., *Physics and chemistry of the upper atmosphere*, Cambridge University Press, 1989.
- Rodriguez, J. V., and U. S. Inan, Electron density changes in the nighttime *D* region due to heating by very-low-frequency transmitters, *Geophys. Res. Lett.*, *21*, 93, 1994.
- Roussel-Dupré, R. A., A. V. Gurevich, T. Tunnel, and G. M. Milikh, Kinetic theory of runaway breakdown, *Phys. Rev.*, *49*, 2257, 1994.
- Roussel-Dupré, R. A., and A. V. Gurevich, On runaway breakdown and upward propagating discharges, *J. Geophys. Res.*, *101*, 2297, 1996.
- Roussel-Dupré, R., E. Symbalisty, Y. Taranenko, and V. Yukhimuk, Simulations of high-altitude discharges initiated by runaway breakdown, *J. Atmos. Sol. Terr. Phys.*, *60*, 917, 1998.

- Sentman, D. D., E. M. Wescott, D. L. Osborne, D. L. Hampton, and M. J. Heavner, Preliminary results from the Sprites94 campaign: Red sprites, *Geophys. Res. Lett.*, *22*, 1205, 1995.
- Shemansky, D. E., and A. L. Broadfoot, Excitation of  $N_2$  and  $N_2^+$  systems by electrons. II: Excitation cross sections and  $N_2$ 1PG low pressure afterglow, *J. Quant. Spectrosc. Radiat. Transfer.*, *11*, 1401, 1971.
- Stolzenburg, M., W. D. Rust, B. F. Smull and T. C. Marshall, Electrical structure in thunderstorm convective regions. 1. Mesoscale convective systems, *J. Geophys. Res.*, *103*, 14059, 1998a.
- Stolzenburg, M., W. D. Rust and T. C. Marshall, Electrical structure in thunderstorm convective regions. 2. Isolated storms, *J. Geophys. Res.*, *103*, 14079, 1998b.
- Symbalysty, E. M. D., R. A. Roussel-Dupré, and V. A. Yukhimuk, Finite volume solution of the relativistic Boltzmann equation for electron avalanche rates, *IEEE Trans. Plasma Sci.*, *26*, 1575, 1998.
- Taranenko, Y. and R. Roussel-Dupré, High altitude discharges and gamma-ray flashes: A manifestation of runaway air breakdown, *Geophys. Res. Lett.*, *23*, 571, 1996.
- Vallance Jones, A., *Aurora*, D. Reidel Publishing Co., Dordrecht, 1974.
- Van Zyl, B., and W. Pendleton, Jr.,  $N_2^+(X)$ ,  $N_2^+(A)$ , and  $N_2^+(B)$  production in  $e^- + N_2$  collisions, *J. Geophys. Res.*, *100*, 23755, 1995.
- Vampola, A. L., Comment on ‘Are fast atmospheric pulsations optical signatures of lightning-induced electron precipitation?’ by J. LaBelle, *Geophys. Res. Lett.*, *15*, 633, 1988.

Volland, H., *Atmospheric Electrodynamics*, Springer-Verlag, New York, 1984.

Vonnegut, B., and C. B. Moore, Giant electrical storms, in *Recent Advances in Atmospheric Electricity*, ed. L. G. Smith, Pergamon Press, New York, 1958

Wilson, C. T. R., The electric field of a thundercloud and some of its effects, *Phys. Soc. London Proc.*, 37, 32D, 1925.

Winckler, J. R., R. C. Franz, and R. J. Nemzek, Fast low-level light pulses from the night sky observed with the SKYFLASH program, *J. Geophys. Res.*, 98, 8775, 1993.

Wolf, T. G. and U. S. Inan, Path-dependent properties of subionospheric VLF amplitude and phase perturbations associated with lightning, *J. Geophys. Res.*, 95, 20997, 1990.

---

N. G. Lehtinen, U. S. Inan, and T. F. Bell, STAR Laboratory, Stanford University, Stanford, CA 94305

Received \_\_\_\_\_

**Figure 1.** Schematics of electrons going from one hemisphere to another. (a) Configuration of the discharge. (b) Electron beam traveling in the magnetosphere from a thunderstorm occurring somewhere in North America to a geomagnetically conjugate location in the southern hemisphere, where it precipitates.

**Figure 2.** The minimum radius  $a_{\min}$  of a disk charge configuration for  $h_+ = 10$  and 15 km.

**Figure 3.** The electron density entering the ionosphere for point and disk charge configurations, calculated in the assumption of vertical geomagnetic field: (1)  $h_+ = 10$  km, point charge; (2)  $h_+ = 10$  km, disk charge; (3)  $h_+ = 15$  km, point charge; (4)  $h_+ = 15$  km, disk charge. The case of non-vertical geomagnetic field is discussed in the text.

**Figure 4.** The momentum distribution of runaway electrons entering the ionosphere above the thunderstorm: the Monte Carlo result and the analytical (log-normal) fit.

**Figure 5.** The optical emissions due to precipitation of runaway electrons in the conjugate hemisphere: (a) the emission rate of First Positive  $N_2$  band, (b) time-integrated emissions in molecular bands. The precipitating electron flux was taken to have a density of  $N_{\text{precip}} \simeq 10^4 \text{ m}^{-3}$ , lasting for 1 ms, corresponding to the initial runaway electron density of  $N_R = 10^5 \text{ m}^{-3}$ .

**Figure 6.** The comparison of energy deposition by the beam of runaway electrons above a thunderstorm and the downcoming precipitating beam in the conjugate hemisphere.

**Figure 7.** Initial ionization and conductivity change due to precipitation of runaway electrons in the conjugate hemisphere.

**Figure 8.** Ionization as a function of time at altitudes 70 and 80 km.

**Figure 9.** Gamma rays emitted by precipitating electrons: (a) cartoon depicting the detection of photons by the satellite; (b)  $\gamma$ -photon energy spectrum; (c) the photon flux as a function of radial distance of  $\gamma$ -ray photons with energies  $\mathcal{E}_{\text{ph}} > 5$  keV, at 500 km altitude; (d) the temporal structure of the photon flux with energies  $\mathcal{E}_{\text{ph}} > 5$  keV, at 500 km altitude directly above the precipitation point, assuming the a square pulse of precipitating electrons with duration of 1 ms.

**Table 1.** Molecular optical band information.

Molecule	Name	Short name	Transition	$(\Lambda)^{-1}$	Quenching agent	$\Gamma, \text{m}^3\text{s}^{-1}$
$\text{N}_2$	First Positive	1P	$B^3\Pi_g \rightarrow A^3\Sigma_u^+$	$6 \mu\text{s}$	air	$5.2 \times 10^{-17}$
$\text{N}_2$	Second Positive	2P	$C^3\Pi_u \rightarrow B^3\Pi_g$	50 ns	air	$7.4 \times 10^{-17}$
$\text{N}_2^+$	First Negative	1N	$B^2\Sigma_u^+ \rightarrow X^2\Sigma_g^+$	70 ns	air	$4 \times 10^{-16}$
$\text{N}_2^+$	Meinel	M	$A^2\Pi_u \rightarrow X^2\Sigma_g^+$	$14 \mu\text{s}$	air	$7 \times 10^{-16}$
$\text{O}_2^+$	First Negative	1N	$b^4\Sigma_g^- \rightarrow a^4\Pi_u$	$1.2 \mu\text{s}$	$\text{N}_2$	$2 \times 10^{-16}$

This table contains the band groups summary and lifetimes  $(\Lambda)^{-1}$ , dominant quenching agents and quenching coefficients  $\Gamma$  of the upper level. The lifetimes are from *Vallance Jones* [1974, p. 119]. See text (Appendix B) for the quenching coefficient references.



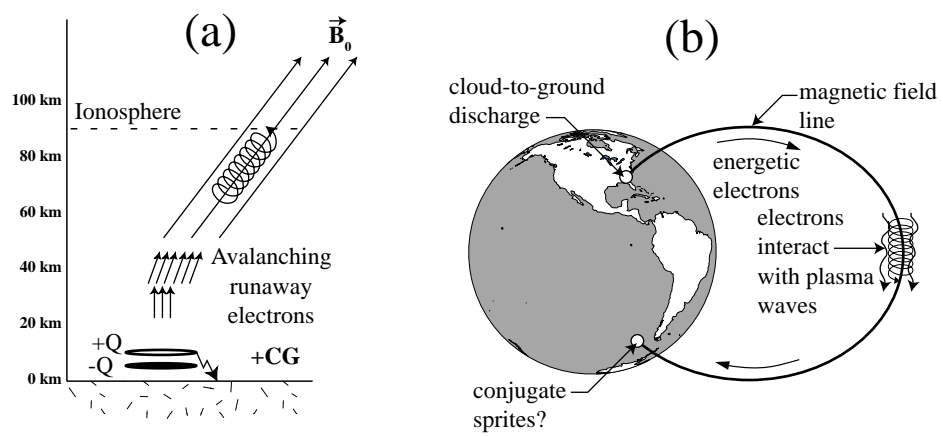


**FIGURE 1**

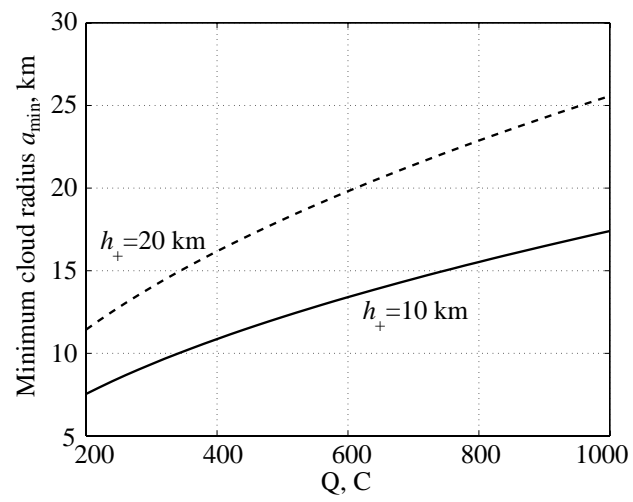


**FIGURE 2**

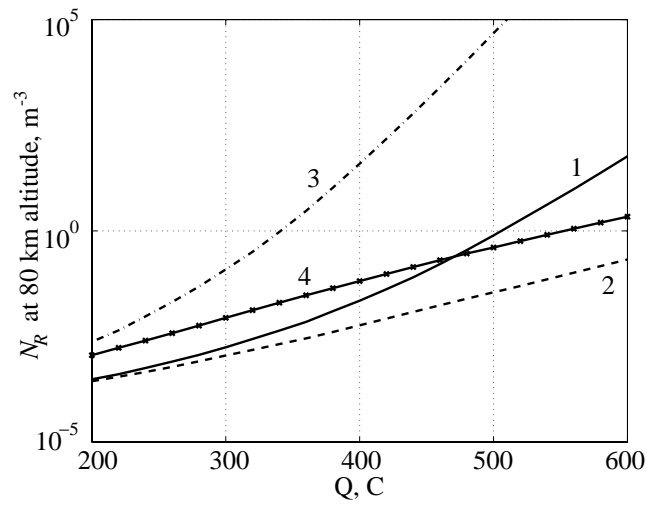


**FIGURE 3**

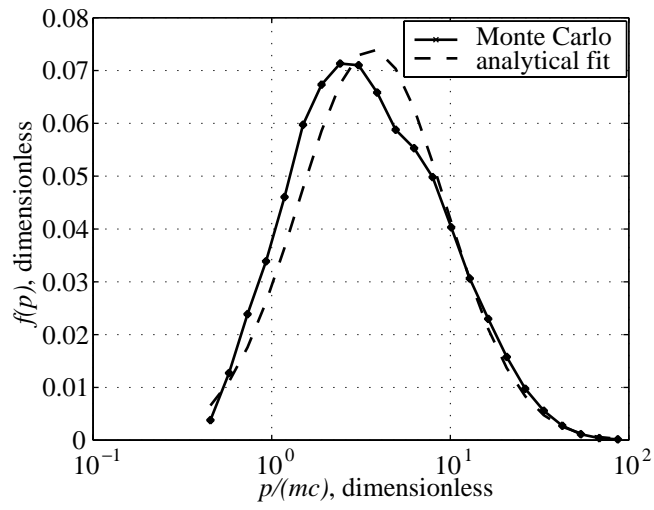


**FIGURE 4**

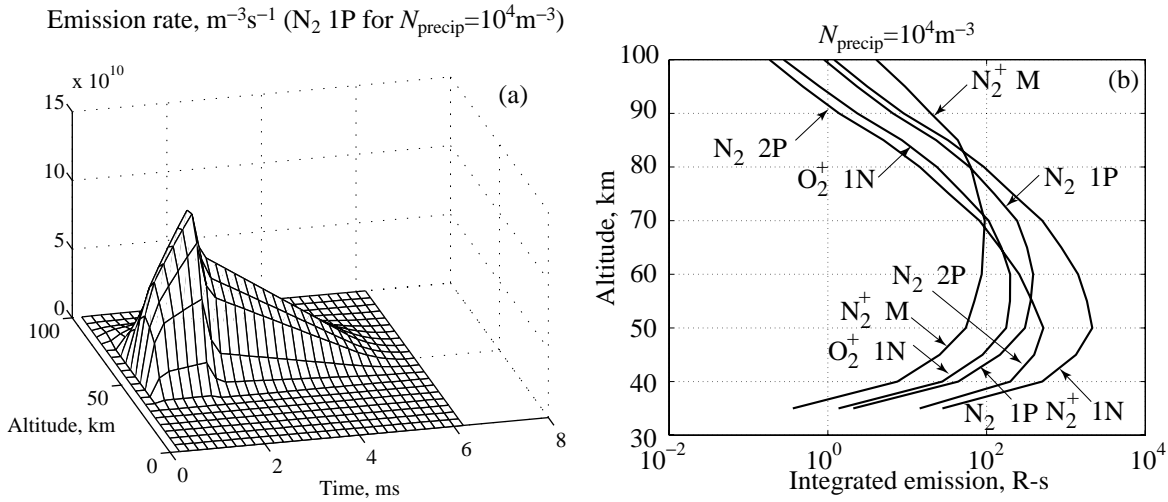


**FIGURE 5**

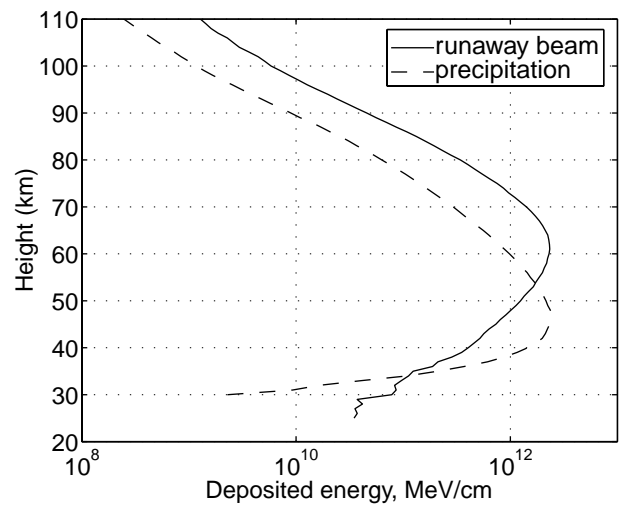


**FIGURE 6**

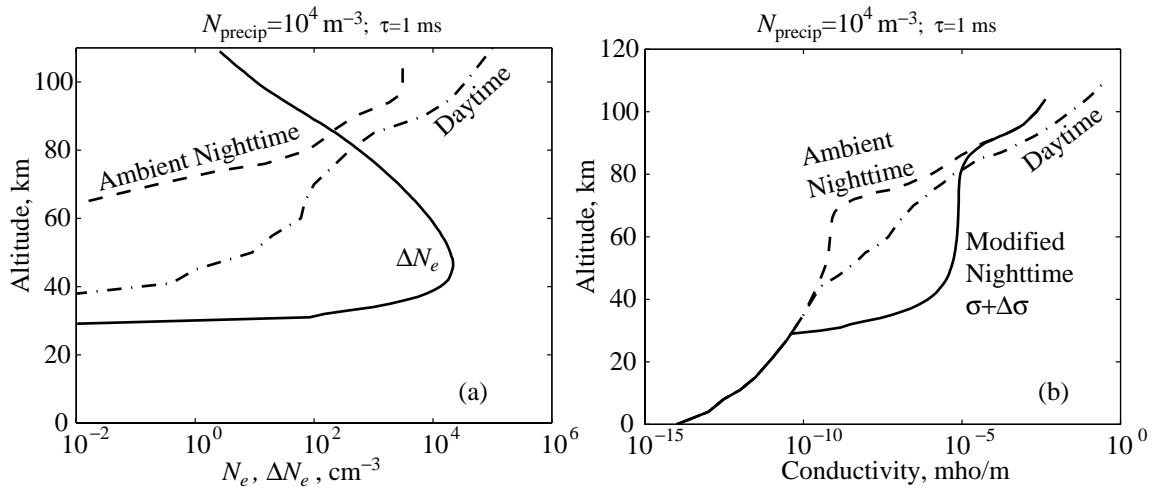


**FIGURE 7**

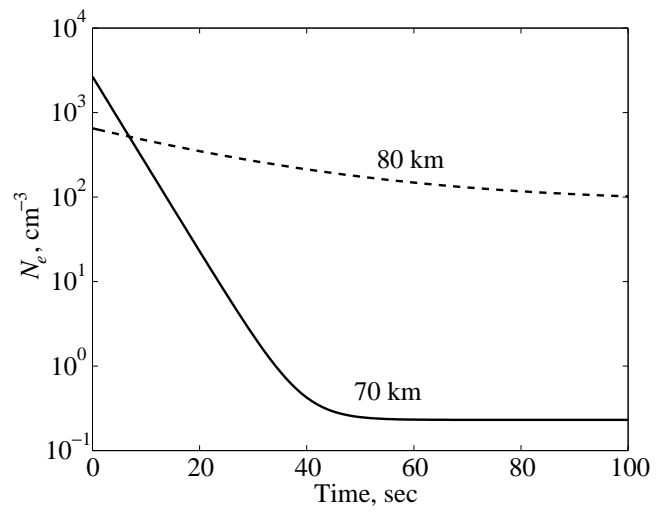


**FIGURE 8**



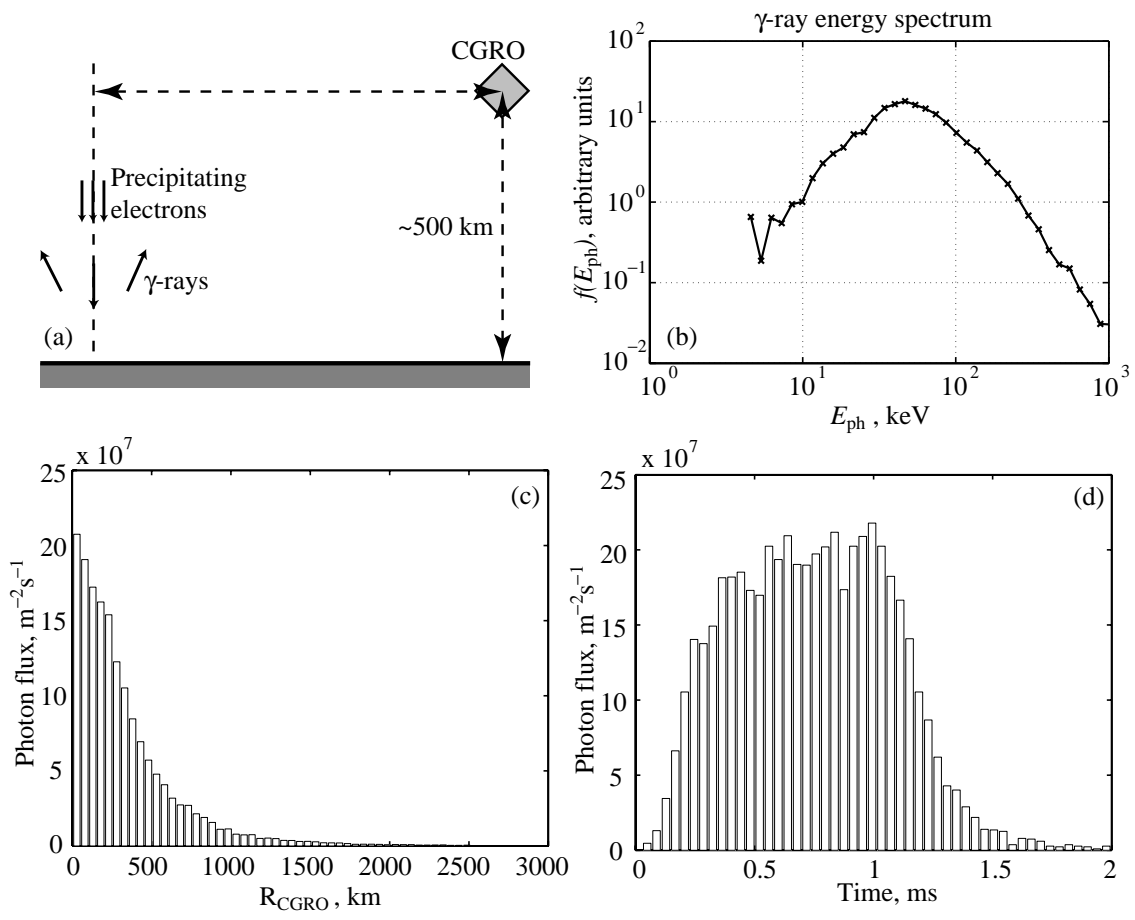


**FIGURE 9**